

This paper is a non-peer reviewed preprint submitted to EarthArXiv.

2 Spatiotemporal forecast of extreme events in a
3 dynamical model of earthquake sequences

4 Hojjat Kaveh,^{1*} Jean-Philippe Avouac,^{1,2} Andrew M Stuart³

¹ Mechanical and Civil Engineering, California Institute of Technology, Pasadena, CA, USA

² Geology and Planetary Science, California Institute of Technology, Pasadena, CA, USA

³ Computing and Mathematical Science, California Institute of Technology, Pasadena, CA, USA

*Corresponding author; E-mail: hkaveh@caltech.edu.

5 **Short title (47 char):**

6 **Forecast of extreme events in earthquake cycles**

7 **One-Sentence Summary (124 char):**

8 **We find statistically feasible and critical prestress distributions and use them to forecast**
9 **large events in space and time.**

10 This paper is a non-peer reviewed preprint submitted to EarthArXiv.

11 **Abstract: Seismic ('earthquakes') and aseismic ('slow earthquakes') slip events**
12 **result from episodic slips on faults and are often chaotic due to stress hetero-**
13 **geneity. Their predictability in nature is a widely open question. Here, we**
14 **forecast extreme events in a numerical model of a single fault governed by**
15 **rate-and-state friction, which produces realistic sequences of slow events with**
16 **a wide range of magnitudes and inter-event times. The complex dynamics of**
17 **this system arise from partial ruptures. As the system self-organizes, prestress**
18 **is confined to a chaotic attractor of a relatively small dimension. We identify**
19 **the instability regions (corresponding to particular stress distributions) within**
20 **this attractor which are precursors of large events. We show that large events**
21 **can be forecasted in time and space based on the determination of these insta-**
22 **bility regions in a low-dimensional space and the knowledge of the current slip**
23 **rate on the fault.**

24 **Introduction**

25 Earthquakes and Slow Slip Events (SSEs) result from episodic frictional slip on the faults. Each
26 slip event releases the elastic strain accumulated during an interevent period during which the
27 fault is locked. This principle is often referred to as the elastic rebound theory in reference
28 to (1). While the elastic rebound theory offers valuable insights into the long-term mean recur-
29 rence time of earthquakes and can be used for time-independent earthquake forecasting (2, 3),
30 it falls short of predicting the time or the magnitude of the larger events (4). The difficulty is
31 that earthquakes often exhibit a chaotic behavior which is manifest in the irregular and rare oc-
32 currence of large slip events and various empirical scaling laws, such as the Gutenberg-Richter
33 and the Omori laws (5). The Gutenberg-Richter law (6) states that earthquake magnitudes are
34 distributed exponentially (the number of earthquakes with magnitude larger than M , $N(M)$, is

35 given by $\log_{10} N(M) = a - bM$, where b is a scaling parameter of the order of one and a is a
36 constant). The Omori law (7) states that the rate of earthquakes during an aftershock sequence
37 decays as $1/t$ where t is the time since the mainshock. Chaotic behavior has also been identified
38 in sequences of ‘slow earthquakes’ in Cascadia (8). These events obey the same scaling laws as
39 regular earthquakes and produce very similar crack-like and pulse-like ruptures, although with
40 several orders of magnitudes smaller slip rate and stress drop (9).

41 The main source of complexities in earthquake sequences is due to stress heterogeneities
42 which can either be of static origin (due to faults geometry (10), roughness (11, 12), or hetero-
43 geneity of mechanical properties (13)) or dynamic, due stress transfers among faults or within
44 a single fault (14). As the stress evolves during the earthquake cycle, it generates asperities and
45 barriers that can either facilitate a complete rupture of a fault (a system-size rupture) or impede
46 the propagation of a rupture, resulting in a partial rupture. Partial or complete ruptures of a
47 fault system are therefore observed in nature (15). Large ruptures, though rare according to the
48 Gutenberg-Richter law, hold greater significance from a seismic hazard perspective.

49 Advances in the understanding of fault friction (16) and in numerical modeling of earthquake se-
50 quences (17, 18) now make it possible to produce realistic simulations (19). While such models
51 are typically presented for arbitrary initial conditions, it is crucial to recognize that certain ini-
52 tial conditions hold more statistical relevance than others during the evolution of the dynamical
53 system. For example, (20) and (21) advocate for conducting simulations over multiple seis-
54 mic cycles to mitigate the influence of arbitrary choices in initial conditions. In fact, the space
55 of feasible stress distributions on a fault during earthquake cycles is significantly smaller than
56 the space of arbitrary initial conditions, as the dynamical system self-organizes into a chaotic
57 attractor (14). When a dynamical system converges to its chaotic attractor, any state outside
58 this attractor is not feasible within the system’s evolution. Consequently, the space of feasible
59 states is limited to the attractor itself, resulting in a significantly smaller domain compared to

60 the space of any arbitrary states for the system.

61 Large events happen rarely in the chaotic evolution of the earthquake cycle so their forecast
62 is extremely challenging. We hypothesize that as for other types of dynamical systems that
63 produce extreme (or rare) events (22, 23), the trajectory of the dynamical system must traverse
64 specific instability regions within the chaotic attractor for large fault ruptures to occur. These
65 instability regions correspond to the optimal distributions of stress (or the states of the frictional
66 interface) that facilitate large ruptures and are also accessible during the evolution of the system
67 because they are part of the chaotic attractor. Despite considerable research on deterministic
68 chaos in earthquake cycle models (24–28), certain essential features of the chaotic attractor,
69 particularly modes relevant to instability that are also statistically feasible, have remained elu-
70 sive in the literature. This is primarily due to the high-dimensional, chaotic, and multi-scale
71 nature of the problem, as well as the rarity of large events.

72 The identification of the optimal state of the frictional interface (prestress) that promotes large
73 events, out of all the statistically feasible distributions is the primary focus of this study. Follow-
74 ing the approach of (29), we use an approximation of the chaotic attractor of the system during
75 the inter-event period; this approximation uses Proper Orthogonal Decomposition (POD) to re-
76 duce dimension and account for the feasibility constraint. Representing the optimal prestress
77 in a low dimensional space is favorable for the purpose of earthquake forecasting, as the data
78 to constrain the physical parameters and current states of the system are sparse for earthquake
79 cycles. We use the proximity of the current slip rate of the system to the slip rates of optimal
80 solutions to propose an effective forecast method of large events. Our results suggest that this
81 framework can be used to both predict events in space and time.

82 As our case study, we use a quasi-dynamic model with the standard rate-and-state friction with
83 the aging law (30). We apply this methodology to a 2D fault within a 3D medium, using a
84 model setup analog to a model that has been shown to produce a realistic sequence of slow

85 earthquakes similar to those observed in Cascadia (31). We limit the analysis to the case of
 86 slow earthquakes as in that case a quasi-dynamic approximation is justified which speeds up the
 87 numerical simulations (32, 33).

88 **Results**

89 **Extreme events formulation**

90 We use a quasi-dynamic model of slip events on a 2D finite fault in a 3D elastic medium, as-
 91 suming rate-and-state friction with the aging law (reviewed in Supp A). The dynamical system
 92 describes the coupled evolution of two functions $V((x, y), t) : \Gamma \times \mathbb{R}^+ \rightarrow \mathbb{R}^+$ and $\theta((x, y), t) :$
 93 $\Gamma \times \mathbb{R}^+ \rightarrow \mathbb{R}^+$. $V((x, y), t)$ is the slip rate, and $\theta((x, y), t)$ is the state variable associated with
 94 the rate-and-state friction law, on the fault surface Γ at time $t \in \mathbb{R}^+$. We assume $u = [V, \theta]^\top$
 95 belongs to an appropriately chosen function space $\mathcal{U} : (\Gamma \times \mathbb{R}^+) \times (\Gamma \times \mathbb{R}^+) \rightarrow \mathbb{R}^+ \times \mathbb{R}^+$ and
 96 characterizes the state of the frictional interface at any given time and position on the fault. In
 97 the context of rate-and-state friction, shear stress is a function of the combination of variables
 98 (V, θ) . Also, the evolution of the system is better rendered in the $\log_{10} u$ space. Consequently,
 99 we use the term ‘prestress’ to refer to the spatial distribution of $w = [\log_{10} V, \log_{10} \theta]^\top$ before a
 100 rupture; nonetheless, we formulate the dynamical model in terms of $u = (V, \theta)$.

101

102 The dynamical system for u is both multi-scale and chaotic and produces ruptures with a
 103 variety of sizes. The governing equation is

$$\frac{\partial u}{\partial t} = \mathcal{N}(u) \tag{1a}$$

$$u(x, y, 0) = u_0(x, y), \quad \forall (x, y) \in \Gamma \tag{1b}$$

104 where \mathcal{N} is a nonlinear differential operator¹ that encompasses the elastodynamics and the

¹Technically a pseudo-differential operator

105 friction law. We denote S^t as the solution operator for the dynamical system, mapping the
 106 current state forward by t time-units:

$$u(x, y, t) = S^t(u(x, y, 0)); \quad (2)$$

107 we can break this map into the components S_V^t and S_θ^t :

$$S^t(u(x, y, 0)) = [S_V^t(u(x, y, 0)), S_\theta^t(u(x, y, 0))]^\top \quad (3)$$

108 We assume that the dynamical system has a global attractor \mathcal{A} on which the dynamics are
 109 chaotic; we refer to this as the chaotic attractor in what follows.

110 Inspired by (23), we define event set $E(V_{\text{thresh}})$ for a prescribed threshold $V_{\text{thresh}} \in \mathbb{R}^+$ as:

$$E(V_{\text{thresh}}) = \{u \in \mathcal{U} : \sup_{(x,y) \in \Gamma} V(x, y) \geq V_{\text{thresh}}\} \quad (4)$$

111 By setting a proper event threshold (V_{thresh}), the event set includes both partial and full ruptures.
 112 In practice, we consider a planar thrust fault that is loaded at a constant rate and consists of a
 113 Rate-Weakening (RW) patch (dotted area in Fig 1 (a)), within which ruptures can nucleate and
 114 propagate, surrounded by a rate-strengthening (RS) patch where the propagation of seismic
 115 ruptures is inhibited (Fig 1 (a)). For details on the physical model see Supp A. In short, we
 116 use a quasi-dynamic approximation of the elastodynamic with rate-and-state friction with aging
 117 law for the state variable. The numerical simulations are run with the QDYN code which is an
 118 open-source boundary element software package to simulate earthquake sequences (34). The
 119 model, with properly selected parameters and initial conditions, exhibits a complex sequence of
 120 events with a variety of magnitudes distributed with a heavy tail consistent with the Gutenberg-
 121 Richter law (Fig 1 (b)). The shear stress on the fault (Fig 1 (c)) increases when the fault is
 122 locked, leading to elastic strain energy build-up in the surrounding elastic medium. During
 123 episodic slip events, the shear stress on the fault drops, and elastic strain energy is released
 124 and dissipated by frictional sliding and the radiation of seismic waves (Fig 1 (c)). The time

125 series of the sequence of partial rupture with rare large ruptures is plotted in Fig 1 (c,d). Since
 126 stress is a function of θ and V in the rate-and-state friction, and θ is not measurable, we do not
 127 have access to stress distribution directly. As a result, in this work, we only assume that we
 128 have observations of the current slip rate when performing extreme event forecasting. The slip
 129 potency deficit, which is the difference between the slip potency (integral of slip on the fault)
 130 and the slip potency if the fault was uniformly slipping at the loading rate, is plotted to show
 131 the chaotic behavior of the system and the rare occurrence of large events. The potency deficit
 132 builds up during the interevent period and drops during the episodic slip events (Fig 1 (e)). The
 133 time series of the magnitude of events is also plotted in Fig 1 (f).

134 We now seek to determine the optimal feasible distributions of $\log_{10} u$ (prestress) in the
 135 interevent period that for a prediction horizon T lead to large magnitude events. By a ‘feasible’
 136 prestress, we mean a prestress that is inside the chaotic attractor of the system; a combination
 137 of V and θ that is likely to be realized during the evolution of the dynamical system. We also
 138 want our criteria for optimality of prestress to be low-dimensional so that it can be captured
 139 using observations that are typically sparse in reality. We then use our low-dimensional critical
 140 prestress and only the current measurable state of the system (slip rate, which can in principle
 141 be estimated from geodetic measurements) to forecast the time and location of a possible large
 142 event in a time window horizon.

143 To formulate the question in mathematical terms, we introduce the moment magnitude of fault
 144 slip cumulated over the duration of integration Δt .

$$\widetilde{M}(u; \Delta t) = \frac{2}{3} \log_{10} \left(G \int_0^{\Delta t} \int_{\Gamma} S_V^t(u(x, y, \cdot)) dx dy dt \right) - 6. \quad (5)$$

145 where G is the elastic shear modulus. \widetilde{M} measures the energy released on the fault in the
 146 \log_{10} scale during Δt time-units (5). \widetilde{M} is slightly different from the definition of the moment
 147 magnitude (M) for one event because in \widetilde{M} , we take Δt to be a constant rather than being

148 the actual duration of a particular event. In practice, we set it to be larger than the longest
 149 duration of events in our model. While we make use of \widetilde{M} in our problem setup and benefit
 150 from its continuity over u , we will report the performance of the forecast of extreme events with
 151 a regular definition of moment magnitude (M).

152 We next define a cost function:

$$F(u; \Delta t, T) = \sup_{t \in [0, T]} \widetilde{M}(S^t(u); \Delta t) \quad (6)$$

153 where function $F : \mathcal{U} \rightarrow \mathbb{R}$ takes u as input and, for a prescribed prediction horizon (T) and
 154 event duration (Δt), finds the largest moment magnitude generated by the initial condition u .
 155 The optimal (most dangerous) feasible prestress conditions are determined by finding the local
 156 maxima (U^*) of $F(u; \Delta t, T)$ over $u \in \mathcal{A} \setminus E(V_{\text{thresh}})$ through an optimization process:

$$U^* = \{u^* | u^* \in \mathcal{A} \setminus E(V_{\text{thresh}}), u^* \text{ is a local maximizer of } F(u; \Delta t, T), F(u^*; \Delta t, T) > F_e^*\} \quad (7)$$

157 where F_e^* is some threshold for the magnitude to define a ‘large’ event. Eq (7) encompasses
 158 the main question of this work; that is finding optimal and statistically feasible prestress on
 159 the fault during the interevent period that makes large events in a short time window. In Eq
 160 (7), $u^* \in \mathcal{A} \setminus E(V_{\text{thresh}})$ ensures that u^* is inside the chaotic attractor (statistical feasibility
 161 constraint) and also in the interevent period; any state (u^*) outside $\mathcal{A} \setminus E(V_{\text{thresh}})$ is inaccessible
 162 during the system’s evolution because of the self-organization. After solving the optimization
 163 problem (Eq (7)), we use the ‘similarity’ of the current states of the system to solutions of
 164 Eq (7), as an indicator of an upcoming large event. We use the current slip rate as our only
 165 knowledge of the current state of the system as θ is not measurable. Solutions to Eq (7) are
 166 instability regions inside the chaotic attractor that generate large ruptures within the time span
 167 of $[0, T]$.

168 Set $\mathcal{A} \setminus E(V_{\text{thresh}})$ is a complicated set in the high-dimensional function space \mathcal{U} . Even if we

169 can solve this optimization problem in this large space, it would be impractical to represent
170 prestress in this high-dimensional space because the sparse data generally available in reality
171 can only yield a low-dimensional model of the slip rate distribution on a fault. As a result, we
172 approximate this set with a simpler set, characterized in a low-dimensional space using the POD
173 method. This approach is developed in the next part.

174 **Model reduction and forecast scheme**

175 Many high-dimensional chaotic dynamical systems can be approximated by a low-dimensional
176 system (35–38). Although the underlying dynamics of earthquakes and Slow Slip cycles are
177 often chaotic (24–28), in certain examples, it has been observed that the chaotic attractors are
178 low dimensional (8, 39) which mathematically implies that we can approximate the evolution
179 of the sequence of events using parameters in a finite-dimensional space instead of an infinite
180 function space. We use this property to reduce the dimensionality and approximate the chaotic
181 attractor during the interevent period.

182 We approximate and reduce the dimensionality of the chaotic attractor of the system during
183 the inter-event period using the POD technique. The POD approach is widely adopted in the
184 study of turbulent fluid flow (35); it is a linear model reduction method based on the singular
185 value decomposition of the data covariance matrix. The modes are ordered by the variance
186 they capture in a dataset consisting of snapshot time series of the field. Since the evolution
187 of the system is better realized in the $w = \log_{10} u$ space, we apply the POD on the w rather
188 than u . We denote by \bar{w} the time average of the field (w) during the interevent period. POD
189 technique inputs snapshots of $w - \bar{w}$ during the interevent period and gives orthonormal basis
190 functions $\phi_i : \Gamma \times \Gamma \rightarrow \mathbb{R} \times \mathbb{R}$ and their associated variance λ_i for $i \geq 1$ where $\lambda_1 > \lambda_2 > \dots$
191 which quantifies the statistical importance of each mode in the dataset. Then we can describe
192 w , and consequently u , using a new coordinate system with the basis functions defined by ϕ_i 's.

193 Since the basis functions are ordered by the variance they capture in the data, the truncation and
 194 approximation of the field $w - \bar{w}$, with the first N_m POD modes captures a maximal statistical
 195 relevance (in the variance sense) of data between all possible N_m dimensional linear subspaces
 196 of $\log_{10} \mathcal{U}$.

197 We approximate $w : w \in \log_{10} (\mathcal{A} \setminus E(V_{\text{thresh}}))$ as perturbations around the time-average of
 198 w during the interevent period ($\bar{w} = [\bar{w}^V, \bar{w}^\theta]$) along those basis functions. Since we want to
 199 approximate only the interevent period we should exclude the event period ($E(V_{\text{thresh}})$) from
 200 the dataset of snapshots that are used to find POD modes (ϕ_i 's). Following (22), we constrain
 201 the perturbations along those eigenvectors to lie within a hyperellipse with a radius along each
 202 eigenvector proportional to the standard deviation of the data captured by each mode. In other
 203 words, we allow more perturbation along those directions that capture more statistical relevance
 204 in the data. The approximation of the chaotic attractor during the interevent period can be
 205 written as:

$$\log_{10} (\mathcal{A} \setminus E(V_{\text{thresh}})) \approx \left\{ \bar{w} + \sum_{i=1}^{N_m} a_i \phi_i \mid \sum_{i=1}^{N_m} \frac{a_i^2}{\lambda_i} \leq r_0^2 \right\}. \quad (8)$$

206 where ϕ_i 's ($i \geq 1$) are the orthonormal basis functions ordered by the data variance they capture
 207 (λ_i) in the centered dataset of time snapshots of $w - \bar{w}$ excluding the event period $E(V_{\text{thresh}})$.
 208 Here a_i is the amplitude of perturbation along ϕ_i and N_m is the number of basis functions we
 209 keep in our model reduction. The maximum perturbation along each basis function (ϕ_i) is
 210 constrained by the corresponding variance λ_i . One can play with the amplitude of the allowed
 211 perturbation which is represented by r_0 .

212 Then Eq (7), which is an optimization problem in a high-dimensional function space \mathcal{U} , con-
 213 strained on a complicated set $\mathcal{A} \setminus E(V_{\text{thresh}})$, can be approximated as an optimization prob-
 214 lem in a low-dimensional (\mathbb{R}^{N_m}) space constrained within a hyperellipse. To solve the con-
 215 strained optimization problem, we use optimal sampling in the framework of Bayesian opti-

216 mization as it is useful when the objective function is costly to evaluate (40). The optimiza-
 217 tion method is described in Supp C. During the optimization process, we collect all optimal
 218 prestresses ($w^* = [(\log V)^*, (\log \theta)^*]^\top$) in a set W^* that satisfies the feasibility constraint
 219 ($w^* \in \log_{10}(\mathcal{A} \setminus E(V_{\text{thresh}}))$) and has the value of $F(10^{w^*}; \Delta t, T)$ above the threshold F_e^* :

220

$$W^* := \left\{ w^* = \bar{w} + \sum_{i=1}^{N_m} a_i \phi_i \mid \sum_{i=1}^{N_m} \frac{a_i^2}{\lambda_i} \leq r_0^2, F(10^{w^*}; \Delta t, T) > F_e^* \right\}. \quad (9)$$

221 W^* corresponds to the set of all of the prestresses leading to extreme events. To perform the
 222 spatial forecast, we need to record the evolution of each w^* for up to time T .

223 We use the proximity of the current state of the system to optimal states as an indicator of an
 224 upcoming large event. The current state of the system (w) is not measurable because θ is not
 225 measurable. Slip rate is the measurable component in w and we use it as a proxy of the current
 226 state of the system. Then, following (22), we use the maximum cosine similarity between the
 227 \log_{10} of the current slip rate ($\log V(t)$) and all of the optimal slip rates ($\log V_i^*$'s) in the set W^*
 228 as an indicator that signals an upcoming large event.

$$I(t) = \max_i \frac{\langle \log V(t) - \bar{w}^V, \log V_i^* - \bar{w}^V \rangle_{L^2}}{\| \log V(t) - \bar{w}^V \|_2 \| \log V_i^* - \bar{w}^V \|_2} \quad (10)$$

229 where $\langle \cdot, \cdot \rangle_{L^2}$ is the L^2 inner product, \bar{w}^V is the average slip rate during interevent periods in
 230 the dataset, $\log V_i^*$ is the velocity component of the i^{th} optimal prestress (w_i^*), and $\| \cdot \|_2$ is
 231 the L^2 norm. Note that $I(t)$ is only a function of the current slip rate on the fault. Here, we
 232 have assumed we have full access to the slip rate on the fault. In Supp D, we have studied a
 233 scenario in which the slip rate is known at only a few points on the fault. The results are similar
 234 because the slip evolution at neighboring points on the fault is strongly correlated due to elastic
 235 coupling.

236 Extreme event forecast

237 We use a simulation run for a total duration of 2200 years. We exclude the initial 200 years to
 238 eliminate the transient behavior, letting the system converge to its chaotic attractor. To define
 239 the event set (Eq (4)), we set the event threshold $V_{\text{thresh}} = 5 \times 10^{-8} (m/s)$. The time series of the
 240 maximum slip velocity on the fault is plotted in Supp A in which V_{thresh} is denoted by a dashed
 241 line. We use data from $t = 200$ to $t = 1200$ years to perform the model reduction and find basis
 242 functions ϕ_i 's and their corresponding variances λ_i 's. We approximate $\mathcal{A} \setminus E(V_{\text{thresh}})$ using Eq
 243 (8) with a number of modes $N_m = 13$ which capture more than 85% variance of the data (based
 244 on the discussion in Supp B). The mean of the field ($\bar{w} = [\bar{w}^V, \bar{w}^\theta]^\top$) together with the first
 245 four eigenfunctions $\phi_i = [\phi_i^V, \phi_i^\theta]^\top$ for interevent periods for the time range $t \in [200, 1200]$ are
 246 plotted in Fig (2) with \bar{w} as the empirical mean of the interevent states of the system w , ϕ_i^V as
 247 the i^{th} eigenfunction of the $\log_{10} V$ and ϕ_i^θ as the i^{th} eigenfunction of the $\log_{10} \theta$. Using ϕ_i 's and
 248 λ_i 's, we solve the optimization problem which has T (prediction horizon), Δt (event duration),
 249 and r_0 (amount of perturbation around \bar{w}) as hyper-parameters. We set the prediction horizon
 250 to $T = 0.5(\text{year})$ and $\Delta t = 0.25(\text{year})$ as the maximum duration of events in the time window
 251 of $t \in [200, 1200]$. With the increase of T , because of the effect of chaos, the predictability
 252 decreases and we would expect the performance of the algorithm to decrease.

253
 254 The value of r_0 in the Eq (8) controls the size of the hyperellipse which is the constraint
 255 of the optimization problem. We performed the optimization for different values of r_0 . For
 256 perturbations constrained within a small hyperellipse (small r_0), the algorithm does not find
 257 any optimal prestress that leads to a large event. This makes sense because, for small r_0 , w is
 258 close to the \bar{w} which is the average state of w during interevent periods. For very large r_0 , the
 259 approximation of $\mathcal{A} \setminus E(V_{\text{thresh}})$ with a hyperellipse is less valid because we let the perturba-
 260 tion have amplitudes much larger than the standard deviation of each component along each

261 eigenfunction. So, one should find an intermediate r_0 whose values of the cost function at the
262 local maxima are larger but close to the maximum magnitude observed in the dataset. Here,
263 we report results for $r_0 = 3$ which means that we won't let the prestress go outside the total
264 3 standard deviation range from \bar{w} in \mathbb{R}^{N_m} . Unlike (22) that, for a fluid flow problem, found
265 a unique solution for their similar optimization problem, we see convergence to multiple local
266 maxima ($w^* = [(\log V)^*, (\log \theta)^*]^\top$) for different algorithm initiations.

267

268 The average prestress during the interevent period for the RW patch, and the prestress corre-
269 sponding to one of the optimal solutions is plotted in Fig 3 (a,b). The cumulative slip distribution
270 corresponding to the event with magnitude 7.5 led by the optimal prestress is plotted in Fig 3
271 (c). We have plotted the slip rate (V), and the state variable (θ) corresponding to this particular
272 optimal solution, together with the convergence of the optimization algorithm, in Supp C. We
273 record the rupture extent of optimal solutions (a total of 12 local maxima) that have $F_e^* > 7.4$
274 to use for spatial prediction. These optimal prestress distributions are relatively complex with
275 heterogeneities both along the strike and along the dip directions. Because we have only ap-
276 proximated the chaotic attractor by a hyperellipse, the solutions of the optimization problem are
277 unlikely to be exactly observed in the simulation of the dynamical system evolution. However,
278 because the non-linear dynamical system can be linearized locally, it can be assumed that if the
279 system gets close to any of these optimal solutions, due to stress redistributions by events of
280 all sizes, a slip event should follow with a head time (the difference between the current time
281 and the time of occurrence of the large slip event) and a slip distribution close to this optimal
282 solution. We rely on this principle to forecast the time and location of large slip events. It
283 is interesting to note that we don't see any full-system size rupture in the forward simulation.
284 However, if we start from homogeneous initial conditions, we see periodic fault-size ruptures.
285 This solution is probably unstable or stable with a small basin of attraction because a relatively

286 small perturbation from the homogeneous initial condition leads to the convergence of the sys-
287 tem to its chaotic attractor.

288 The indicator $I(t)$ (Eq (10)), can effectively forecast large events for the dataset from $t = 1200$
289 to $t = 2200$ years with a prediction horizon of $T = 0.5$ (year). To illustrate, $I(t)$ is plotted
290 alongside F in Fig 4 (a). A high value of F shows an upcoming large event in the time interval
291 $[0, T]$ and we observe that when F rises, the indicator signals a large event by rising to large
292 values. We define a threshold I_e above which we signal an upcoming large event. We also de-
293 fine F_e as the threshold for extreme events; whenever F is larger than F_e we say that an extreme
294 event is going to happen in the next T year(s). The values of F_e and I_e are determined such that
295 the proportion of the true positive and true negative forecasts of extreme events are maximized.
296 By recording the values of $I(t)$ and $F(t)$, we can empirically find the conditional probability
297 $P(F|I)$ (Fig 4 (b)). Values of F_e and I_e are denoted by the white vertical and horizontal dashed
298 lines in Fig 4 (b). The probability in this context is with respect to the invariant measure of the
299 chaotic attractor. Different quadrants of this plot show four conditions including true negative,
300 false negative, true positive, and false positive from bottom left counterclockwise to top left.
301 While most of the high values of $P(F|I)$ lie inside the true negative and true positive regions,
302 it is essential to acknowledge that the probabilities of false negative and false positive are not
303 zero. We also plot the empirical probability of observing an event greater than F_e given the
304 knowledge of I , ($P[F > F_e|I]$). This value which is denoted by P_{ee} is plotted in Fig 4 (c). P_{ee}
305 consistently rises to values close to one, which is another way to show that the indicator I can
306 be used as a predictor of large events. We plot the forecast of rupture extent in Fig 4 (d) which
307 shows the effectiveness of both spatial and temporal forecasts of large events. Since we have
308 recorded the rupture extent of optimal solutions (elements in set W^*), as soon as the current
309 state of the system gets close to the i^{th} optimal solution and the indicator signals an upcom-
310 ing event ($I(t) > I_e$), we propose the recorded rupture extent of the i^{th} optimal solution as the

311 spatial forecast. Fig 4 (e) shows the temporal forecast of events with the magnitude of events
312 plotted in blue. Whenever the indicator has a value greater than I_e , we forecast (red region)
313 that an event larger than $F_e = 6.9$ (black dashed line) will happen. Red shows the temporal
314 prediction of events larger than F_e . The magnitude in Fig 4 (e) is calculated according to the
315 regular definition of the magnitude of an event (i.e. by integrating the slip velocity above the
316 threshold over the exact duration of the event). In Supplemental Video 1, an animation of this
317 prediction is available.

318 **Discussion**

319 This study demonstrates the possibility of predicting the time, size, and spatial extent of extreme
320 events in a simplified dynamical model of earthquake sequences based on the instantaneous
321 observation of fault slip rate. The proposed approach was adapted from a technique developed
322 to forecast extreme events in turbulent fluid flow (22,29). By constraining the prestress on a fault
323 to the only feasible ones and solving an optimization problem, we found the optimal prestress
324 in a low dimensional space. Optimal prestress refers to configurations of stress heterogeneity
325 on the fault triggering large events within small time windows. Identifying the optimal prestress
326 distributions that are also statistically accessible during the earthquake cycle is pivotal.

327 Prestress self-organizes into a chaotic attractor which occupies only a small fraction of all
328 possible stress distributions on the fault. The identification of the optimal prestress within this
329 reduced set is crucial for two reasons. First, it helps establish a low-dimensional representa-
330 tion of optimal prestress; the significance of reduced-order proxy of critical prestress is even
331 more important for earthquakes than SSEs, primarily due to the scarcity of observational data
332 obtained from paleoseismic records. Second, everything outside this set remains unseen dur-
333 ing the earthquake cycle's evolution. If that was not the case, the space of hypothetical stress
334 distribution possibly leading to large events would be intractable.

335 Our finding shows that the chaotic nature of earthquake sequences is not an insurmountable
336 obstacle to time-dependent earthquake forecasting. However, we acknowledge that we consid-
337 ered a favorable model setup designed to produce slow earthquakes. It would be now interesting
338 to test this approach in the case of a model setup producing regular earthquakes (i.e., with slip
339 rates of $1\text{cm}/s$ to $1\text{m}/s$ to be comparable to real earthquakes) and with a larger range of earth-
340 quake magnitudes. This is doable although computationally challenging. It is expected that
341 earthquake sequences would then show more complexity due to the cascading effects which are
342 responsible for foreshocks and aftershocks in natural earthquake sequences, and which are not
343 present in our simulations. In that regard, (22) reported that the performance of their prediction
344 of rare events diminishes with the increase in Reynolds number in their turbulent flow case. It
345 is possible that we have the same limitation as the ratio of the nucleation size to the dimensions
346 of the fault decreases.

347 **Materials and Methods**

348 We used a model of a 2D thrust fault in a 3D medium governed by RS friction with aging law
349 for the evolution of state variable (θ). The forward model is briefly reviewed in Supp A. The
350 model parameters are summarized in Table S1. To simulate the forward model, we use the
351 [QDYN software](#)², which is an open-source code to simulate earthquake cycles (34). We use
352 the POD technique to reduce the dimensionality of the problem. This method is reviewed in
353 Supp B. To solve the optimization problem we use the Bayesian optimization method (40, 41)
354 that is reviewed in Supp C. We used the open source code available on [GitHub](#)³ for solving the
355 optimization problem.

²<https://github.com/ydluo/qdyn>

³<https://github.com/ablancha/gpsearch>

356 **Supplementary Materials**

357 Supp A Model

358 Supp B Proper Orthogonal Decomposition (POD): method and result

359 Supp C Optimization

360 Supp D Forecast with Partial Observation of Slip Rate

361 Supplemental Figures: Fig S1 to S5

362 Supplemental Videos: Movie S1 to Movie S2

References and Notes

- 364 1. H. Reid, *The Mechanics of the Earthquake, The California Earthquake of April 18, 1906,*
365 *Report of the State Investigation Commission*, vol. 2 (1910).
- 366 2. J.-P. Avouac, *Annual Review of Earth and Planetary Sciences* **43**, 233 (2015). .eprint:
367 <https://doi.org/10.1146/annurev-earth-060614-105302>.
- 368 3. D. Marsan, Y. J. Tan, *Bulletin of the Seismological Society of America* **110**, 874 (2020).
- 369 4. J. Murray, P. Segall, *Nature* **419**, 287 (2002). Number: 6904 Publisher: Nature Publishing
370 Group.
- 371 5. C. H. Scholz, *Mechanics of faulting* (1989). Publication Title: Annual review of earth and
372 planetary sciences. Vol. 17 ISSN: 0084-6597.
- 373 6. B. Gutenberg, C. F. Richter, *MAUSAM* **1**, 174 (1950). Number: 2.
- 374 7. T. Utsu, Y. Ogata, R. S. Matsu'ura, *Journal of Physics of the Earth* **43**, 1 (1995).
- 375 8. A. Gualandi, J.-P. Avouac, S. Michel, D. Faranda, *Science Advances* **6**, eaaz5548 (2020).
376 Publisher: American Association for the Advancement of Science.
- 377 9. S. Michel, A. Gualandi, J.-P. Avouac, *Nature* **574**, 522 (2019). Number: 7779 Publisher:
378 Nature Publishing Group.
- 379 10. P. G. Okubo, K. Aki, *Journal of Geophysical Research: Solid Earth* **92**, 345 (1987). .eprint:
380 <https://onlinelibrary.wiley.com/doi/pdf/10.1029/JB092iB01p00345>.
- 381 11. A. Sagy, E. E. Brodsky, G. J. Axen, *Geology* **35**, 283 (2007).
- 382 12. C. Cattania, *Geophysical Research Letters* **46**, 10384 (2019). .eprint:
383 <https://onlinelibrary.wiley.com/doi/pdf/10.1029/2019GL083628>.

- 384 13. Y. Kaneko, J.-P. Avouac, N. Lapusta, *Nature Geoscience* **3**, 363 (2010). Number: 5 Pub-
385 lisher: Nature Publishing Group.
- 386 14. B. E. Shaw, J. R. Rice, *Journal of Geophysical Research: Solid Earth* **105**, 23791 (2000).
387 _eprint: <https://onlinelibrary.wiley.com/doi/pdf/10.1029/2000JB900203>.
- 388 15. A. O. Konca, *et al.*, *Nature* **456**, 631 (2008). Number: 7222 Publisher: Nature Publishing
389 Group.
- 390 16. C. Marone, *Annual Review of Earth and Planetary Sciences* **26**, 643 (1998). _eprint:
391 <https://doi.org/10.1146/annurev.earth.26.1.643>.
- 392 17. N. Lapusta, J. R. Rice, Y. Ben-Zion, G. Zheng, *Journal of*
393 *Geophysical Research: Solid Earth* **105**, 23765 (2000). _eprint:
394 <https://onlinelibrary.wiley.com/doi/pdf/10.1029/2000JB900250>.
- 395 18. J. R. Rice, N. Lapusta, K. Ranjith, *Journal of the Mechanics and Physics of Solids* **49**, 1865
396 (2001).
- 397 19. S. Barbot, N. Lapusta, J.-P. Avouac, *Science* **336**, 707 (2012). Publisher: American Asso-
398 ciation for the Advancement of Science.
- 399 20. N. Lapusta, J. R. Rice, *Journal of Geophysical Research: Solid Earth* **108** (2003). _eprint:
400 <https://onlinelibrary.wiley.com/doi/pdf/10.1029/2001JB000793>.
- 401 21. A. M. Rubin, J.-P. Ampuero, *Journal of Geophysical Research: Solid Earth* **110** (2005).
402 _eprint: <https://onlinelibrary.wiley.com/doi/pdf/10.1029/2005JB003686>.
- 403 22. P. J. Blonigan, M. Farazmand, T. P. Sapsis, *Physical Review Fluids* **4**, 044606 (2019).
404 Publisher: American Physical Society.

- 405 23. M. Farazmand, T. P. Sapsis, *Applied Mechanics Reviews* **71** (2019).
- 406 24. J. Huang, D. L. Turcotte, *Geophysical Research Letters* **17**, 223 (1990). [.eprint:
407 https://onlinelibrary.wiley.com/doi/pdf/10.1029/GL017i003p00223.](https://onlinelibrary.wiley.com/doi/pdf/10.1029/GL017i003p00223)
- 408 25. T. W. Becker, *Geocomplexity and the Physics of Earthquakes*
409 (American Geophysical Union (AGU), 2000), pp. 5–26. [.eprint:
410 https://onlinelibrary.wiley.com/doi/pdf/10.1029/GM120p0005.](https://onlinelibrary.wiley.com/doi/pdf/10.1029/GM120p0005)
- 411 26. M. Anghel, Y. Ben-Zion, R. Rico-Martinez, *Computational Earthquake Science Part*
412 *I*, A. Donnellan, P. Mora, M. Matsu'ura, X.-c. Yin, eds., Pageoph Topical Volumes
413 (Birkhäuser, Basel, 2004), pp. 2023–2051.
- 414 27. N. Kato, *Bulletin of the Seismological Society of America* **106**, 1772 (2016).
- 415 28. S. Barbot, *Tectonophysics* **768**, 228171 (2019).
- 416 29. M. Farazmand, T. P. Sapsis, *Science Advances* **3**, e1701533 (2017). Publisher: American
417 Association for the Advancement of Science.
- 418 30. A. Ruina, *Journal of Geophysical Research: Solid Earth* **88**, 10359 (1983). [.eprint:
419 https://onlinelibrary.wiley.com/doi/pdf/10.1029/JB088iB12p10359.](https://onlinelibrary.wiley.com/doi/pdf/10.1029/JB088iB12p10359)
- 420 31. L. Dal Zilio, N. Lapusta, J. Avouac, *Geophysical Research Letters* **47** (2020).
- 421 32. J. R. Rice, *Journal of Geophysical Research: Solid Earth* **98**, 9885 (1993). [.eprint:
422 https://onlinelibrary.wiley.com/doi/pdf/10.1029/93JB00191.](https://onlinelibrary.wiley.com/doi/pdf/10.1029/93JB00191)
- 423 33. M. Y. Thomas, N. Lapusta, H. Noda, J.-P. Avouac, *Journal of*
424 *Geophysical Research: Solid Earth* **119**, 1986 (2014). [.eprint:
425 https://onlinelibrary.wiley.com/doi/pdf/10.1002/2013JB010615.](https://onlinelibrary.wiley.com/doi/pdf/10.1002/2013JB010615)

- 426 34. Y. Luo, J. P. Ampuero, P. Galvez, M. v. d. Ende, B. Idini, QDYN: a Quasi-DYNamic
427 earthquake simulator (v1.1) (2017).
- 428 35. K. Taira, *et al.*, *AIAA Journal* **55**, 4013 (2017). Publisher: American Institute of Aeronau-
429 tics and Astronautics.
- 430 36. C. W. Rowley, S. T. Dawson, *Annual Review of Fluid Mechanics* **49**, 387 (2017). _eprint:
431 <https://doi.org/10.1146/annurev-fluid-010816-060042>.
- 432 37. M. Li, S. Jain, G. Haller, *Nonlinear Dynamics* **111**, 8881 (2023).
- 433 38. A. Brandstätter, *et al.*, *Physical Review Letters* **51**, 1442 (1983). Publisher: American Phys-
434 ical Society.
- 435 39. A. Gualandi, D. Faranda, C. Marone, M. Cocco, G. Mengaldo, *Earth and Planetary Science*
436 *Letters* **604**, 117995 (2023).
- 437 40. A. Blanchard, T. Sapsis, *Journal of Computational Physics* **425**, 109901 (2021).
- 438 41. E. Brochu, V. M. Cora, N. de Freitas, A Tutorial on Bayesian Optimization of Expensive
439 Cost Functions, with Application to Active User Modeling and Hierarchical Reinforcement
440 Learning (2010). ArXiv:1012.2599 [cs].
- 441 42. P. H. Geubelle, J. R. Rice, *Journal of the Mechanics and Physics of Solids* **43**, 1791 (1995).

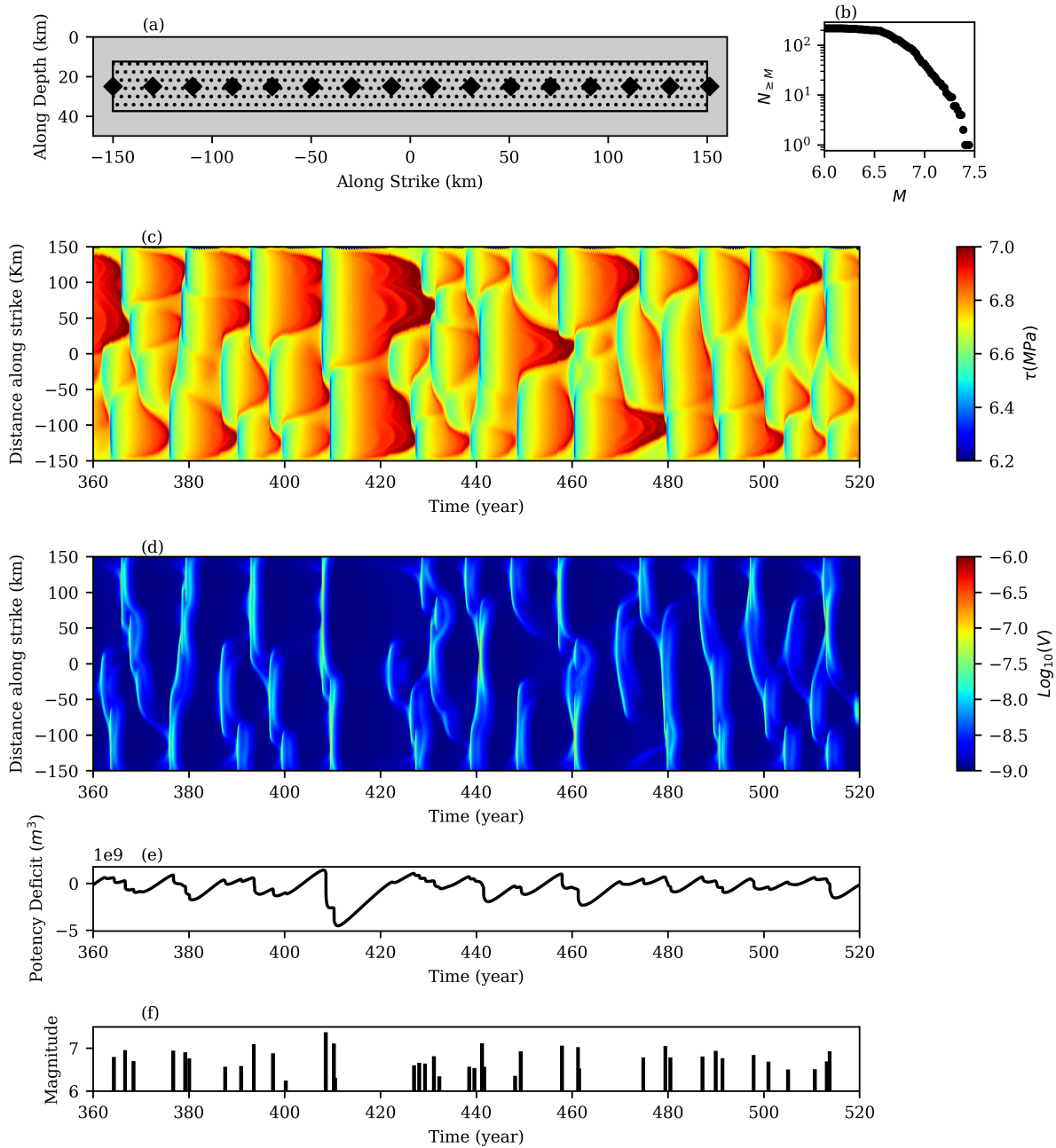


Figure 1: Geometry of the fault (a). The RW patch is the dotted area that is surrounded by the RS patch. The diamonds are the locations of slip rate measurements for the scenario in which we do not have full access to the slip rate on the entire fault. The number of events with a magnitude greater than M , (N_M) is plotted in (b) for 1000 years of simulation time. Maximum stress along the depth for the RS patch is plotted as a function of distance along strike and time (c). The maximum slip rate for the RS patch along the depth is plotted as a function of distance along strike and time (d). The time-series of the potency deficit and magnitudes are plotted in (e) and (f) respectively.

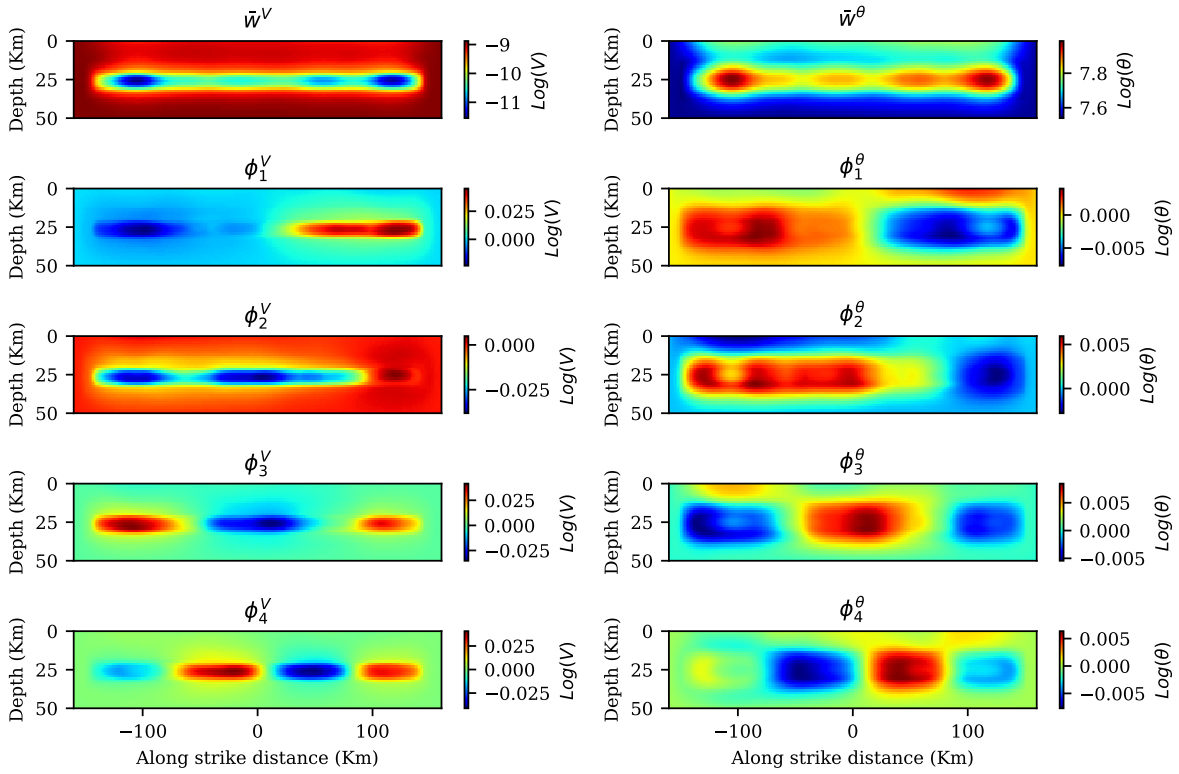


Figure 2: Average of the \log_{10} of slip rate (\bar{w}^V) and state variable (\bar{w}^θ) during the interevent periods, and first four eigenfunctions for \log_{10} of slip rate (ϕ_i^V for $1 \leq i \leq 4$) and state variable (ϕ_i^θ for $1 \leq i \leq 4$) that are ordered by the variance they capture in the datasets. The dataset contains interevent snapshots of \log_{10} of slip rate and state variable during the interevent periods from the year 200 to 1200.

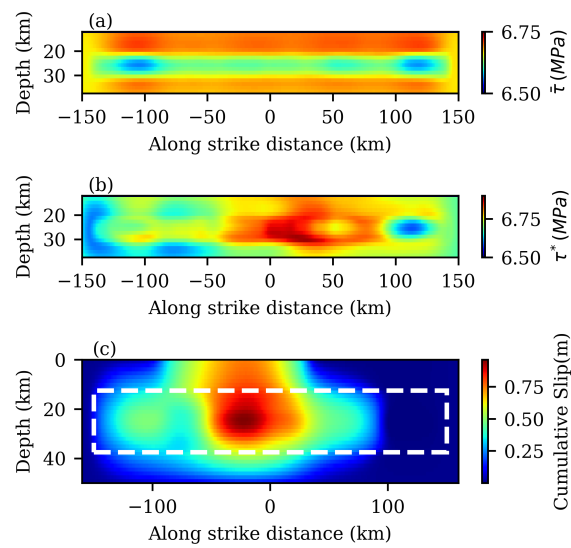


Figure 3: Average of the shear stress on the RW patch of the fault during the interevent period (a). One of the local optimal prestress distributions that leads to an event with a magnitude of 7.5 (b) with its corresponding cumulative slip plotted in (c). To increase the readability (b,c) are plotted only for the RW patch. The RW patch in (c) is denoted by the dashed white line.

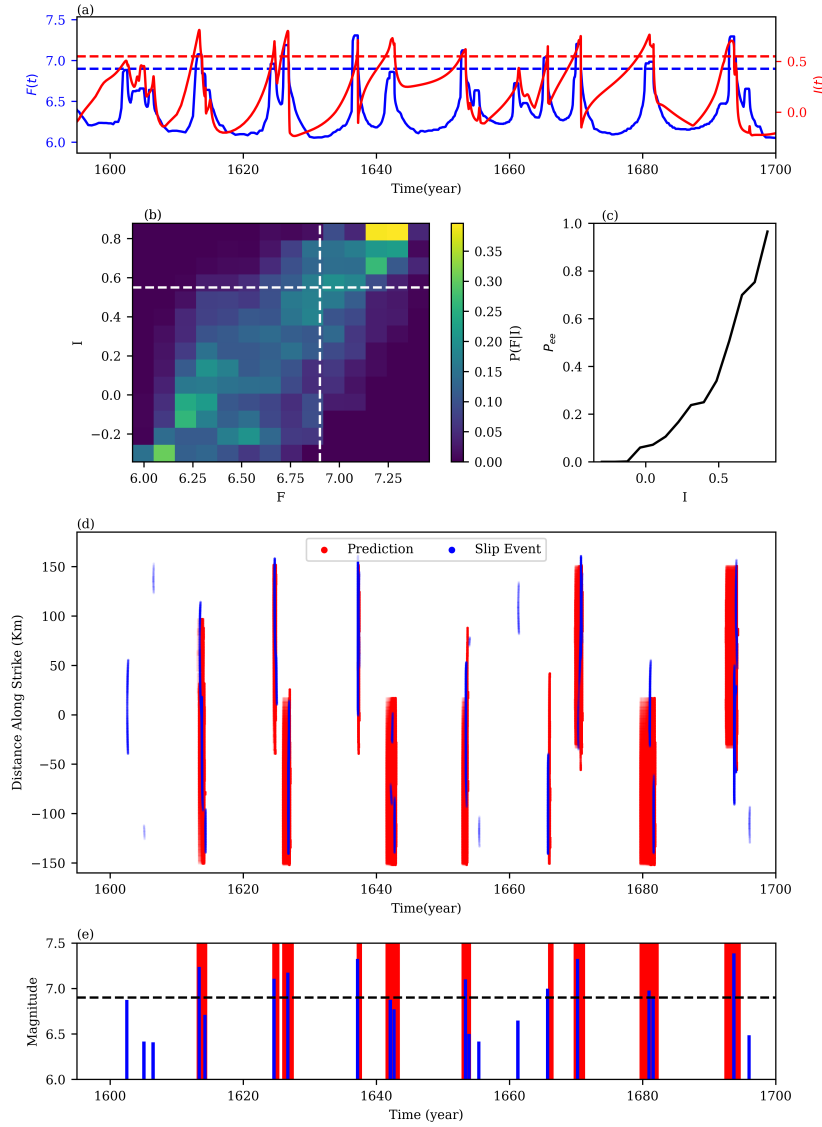


Figure 4: Spatiotemporal prediction of events in 1000 years of data in the test set (data from the year 1200 to 2200). The time series of the functions F and I show that I rises when there is an upcoming large event (F is large), and it goes down when there is no upcoming large event. The blue and red dashed lines correspond to F_e and I_e (a). The empirical conditional probability $P(F|I)$. The vertical and horizontal dashed lines are F_e , and I_e respectively (b). The empirical probability of having an event with the value \tilde{M} greater than F_e in the next 0.5(year) as a function of the value of the indicator I (c). The spatiotemporal prediction of events is plotted by red where blue is the actual events in the dataset (d). Prediction of the magnitudes with the blue bars as the magnitude of events in the dataset. The horizontal axis for the blue bars denotes the time when an event starts. Red regions denote the times of high probability of large events (above magnitude 6.9 (dashed line)) based on our indicator (e).

442 **Acknowledgments**

443 The authors HK and J-PA express their sincere gratitude to the National Science Foundation
444 (NSF) for their financial support of this research project, through the Industry-University Col-
445 laborative Research Center Geomechanics and Mitigation of Geohazards (award #1822214).
446 Author AMS is grateful to DoD for support as a Vannevar Bush Faculty Fellow. Additionally,
447 the authors are grateful for the valuable input and discussion provided by Nadia Lapusta, Bren-
448 dan Meade, Themis Sapsis, Adriano Gualandi, Alba Rodriguez, Camilla Cattania, Elif Oral,
449 Mateo Acosta, Kelian Dascher-Cousineau, Zachary R Ross, Jan Dirk Jansen, Kyungjae Im.

Supporting Information for

**Spatiotemporal forecast of extreme events in a dynamical model of
earthquake sequences**

Hojjat Kaveh,^{1*} Jean-Philippe Avouac,^{1,2} Andrew M Stuart³

¹ Mechanical and Civil Engineering, California Institute of Technology, Pasadena, CA, USA

² Geology and Planetary Science, California Institute of Technology, Pasadena, CA, USA

³ Computing and Mathematical Science, California Institute of Technology, Pasadena, CA,
USA

*Corresponding author; E-mail: hkaveh@caltech.edu.

Supp A Model

We use a model of a 2D thrust fault in a 3D medium governed by RS friction with aging law for the evolution of state variable (θ):

$$\frac{\tau}{\bar{\sigma}_n} = \mu^* + a \ln\left(\frac{V}{V^*}\right) + b \ln\left(\frac{\theta V^*}{D_{RS}}\right), \quad (\text{S1})$$

$$\frac{d\theta}{dt} = 1 - \frac{\theta V}{D_{RS}}. \quad (\text{S2})$$

Here $V(x, y, t) : \Gamma \times \mathbb{R}^+ \rightarrow \mathbb{R}^+$ is slip rate on the fault, $\theta(x, y, t) : \Gamma \times \mathbb{R}^+ \rightarrow \mathbb{R}^+$ is the state variable, $\tau(x, y, t) : \Gamma \times \mathbb{R}^+ \rightarrow \mathbb{R}^+$ is the frictional strength, $\bar{\sigma}_n$ is the effective normal stress, and a, b, D_{RS} are frictional properties of the surface (Γ) and are positive. μ^* and V^* are reference friction and slip rate respectively. The sign of $a - b$ determines the frictional regime of the fault. For $a - b > 0$, the fault is Velocity Strengthening (VS); a jump in the velocity would increase the fault strength. Regions with $a - b > 0$ suppress the rupture nucleation and acceleration. For $a - b < 0$ fault is Velocity Weakening (VW); a jump in the slip rate (V), decreases the strength, and the fault is capable of nucleating earthquakes and accelerating the ruptures. $a - b$ varies spatially and is plotted in Fig 1.

The stress rate on the fault can also be written as:

$$\dot{\tau} = \mathcal{L}(V - V_{pl}) - \frac{G}{2c_s} \dot{V} \quad (\text{S3})$$

where \mathcal{L} is a pseudo-differential operator, and contains most of the elastodynamic response (42). Function $V_{pl}(x, y)$ is the plate slip rate which is assumed to be constant in time in this work. We use quasi-dynamic approximation for \mathcal{L} , ignoring the wave-mediated effects on the fault surface (42). G and c_s are shear modulus and shear wave speed respectively. By taking the time derivative of Eq (S1), and eliminating $\dot{\tau}$ from the equations we have a dynamical system of the form of Eq (1) for $u = [V, \theta]^\top$. We simulate the dynamical system from a non-symmetric initial condition (u_0) for 2200(*yr*) and remove the first 200(*yr*) to not include the transient behavior.

Table S1: Physical Properties

VW region	a	0.004
	b	0.014
VS region	a	0.019
	b	0.014
Characteristic slip weakening distance	D_{RS}	0.045(m)
Reference steady state slip rate	V^*	$10^{-6} \frac{m}{s}$
Reference steady-state friction coefficient	f^*	0.6
Effective normal stress	$\bar{\sigma}_n$	10(MPa)
Shear modulus	G	30(GPa)
Plate loading Velocity	V_{pl}	40(mm/year)

The dynamical system based on this formalism can produce realistic cycles of earthquakes and SSEs. To justify the assumption of ignoring wave propagation effects along the fault, we use a parameter regime that produces SSEs in which V is small enough that the wave effects across the faults are negligible. We use model parameters and geometry used in (31) to simulate SSEs similar to those in Cascadia, except that for simplicity we did not include the effect of pore-pressure dilatancy. We use the QDYN software, which is an open-source code to simulate earthquake cycles (34). The frictional and physical properties of our problem are summarized in Table S1 and Fig 1. The maximum slip rate on the fault is plotted in Fig S1 with the dashed line as the threshold that we use for defining an event.

Supp B Proper Orthogonal Decomposition (POD): method and result

In this section, we review how to reduce the dimension of the dataset consisting of slip rate and state variable using the POD method. We use this method to find critical prestress in a low-dimensional space instead of the high-dimensional function space. Another reason to use this method is because Eq (7) is an optimization problem constrained on the chaotic attractor of the system with the event period excluded. For solving the constraint optimization problem (Eq (7)), one method (29) is to exclude the extreme events from the chaotic attractor and approximate the remaining using the POD technique. Here, we exclude the event period from the dataset to only approximate the interevent period. The method of approximating the chaotic attractor using POD modes is used in different fields. As an example, the work in (22) used 50 POD modes to approximate the chaotic attractor of a turbulent channel flow. One behavioral difference between our model of the earthquake cycle and the turbulent channel flow example is that the time stepping in our problem is adaptive due to the system's multi-scale behavior; there are more sample data when the dynamical system is stiff. However, since we are removing the event period from the data, we only include the slow part of the system in our dataset.

In the following paragraphs, we describe the POD analysis on our dataset of simulations. The dataset comprises snapshots within the time span from the year 200 to 1200 excluding the event set ($E(V_{\text{thresh}})$). We use the time snapshots of discretized states of the system (θ and V) which belong to a high but finite-dimensional space. After discretization, $V : \mathbb{R}^{N_x \times N_y} \times \mathbb{R}^+ \rightarrow \mathbb{R}^+$ and $\theta : \mathbb{R}^{N_x \times N_y} \times \mathbb{R}^+ \rightarrow \mathbb{R}^+$. $N_x = 256$ and $N_y = 32$ are the numbers of grid points along the strike and depth respectively.

Since the evolution of the system is better realized in \log_{10} space, we apply the POD on the \log_{10} of the dataset. We define vectors $w_1(t_k)$ and $w_2(t_k)$ both in $\mathbb{R}^{N_x N_z}$ for time t_k as the vectorized

form of the logarithm of V and θ at time t_k .

$$w_1(t_k) = \log_{10} \left(\begin{bmatrix} V_{1,1} \\ V_{1,2} \\ \vdots \\ V_{1,N_x} \\ V_{2,1} \\ V_{2,2} \\ \vdots \\ V_{2,N_x} \\ \vdots \\ V_{N_z,1} \\ V_{N_z,2} \\ \vdots \\ V_{N_z,N_x} \end{bmatrix} \right)_{t=t_k} \quad (\text{S4})$$

$$w_2(t_k) = \log_{10} \left(\begin{bmatrix} \theta_{1,1} \\ \theta_{1,2} \\ \vdots \\ \theta_{1,N_x} \\ \theta_{2,1} \\ \theta_{2,2} \\ \vdots \\ \theta_{2,N_x} \\ \vdots \\ \theta_{N_z,1} \\ \theta_{N_z,2} \\ \vdots \\ \theta_{N_z,N_x} \end{bmatrix} \right)_{t=t_k} \quad (\text{S5})$$

where for example, by $[V_{i,j}]_{t_k}$, we mean slip rate at i^{th} element along strike and j^{th} element along the depth at k^{th} snapshots in the dataset. Then, we stack pairs of w_1 and w_2 to make a vector w :

$$w(t_k) = \begin{bmatrix} w_1(t_k) \\ w_2(t_k) \end{bmatrix} \in \mathbb{R}^{2N_x N_z}. \quad (\text{S6})$$

We define $\bar{w} = [\bar{w}^V, \bar{w}^\theta]^\top$ as the time average of $w(t_i)$ for all i in the dataset.

$$\bar{w} = \frac{1}{N_d} \sum_{i=1}^{N_d} w(t_i) \quad (\text{S7})$$

where N_d is the total number of snapshots in the dataset. \bar{w}^V and \bar{w}^θ are plotted in Fig 2. We define $p(t_k) = w(t_k) - \bar{w}$ and then we define a matrix $P \in \mathbb{R}^{2N_x N_z \times N_d}$ with the following entries:

$$P = [p(t_1) \ p(t_2) \ \cdots \ p(t_{N_d})] \in \mathbb{R}^{2N_x N_z \times N_d}. \quad (\text{S8})$$

Then, we define the covariance matrix R as the following:

$$R = \frac{1}{(N_d - 1)} P P^T \in \mathbb{R}^{2N_x N_z \times 2N_x N_z} \quad (\text{S9})$$

Now, we can find the eigenvectors of matrix R :

$$R \phi_j = \lambda_j \phi_j \quad \lambda_1 \geq \lambda_2 \geq \cdots \geq \lambda_{2N_x N_z} \geq 0. \quad (\text{S10})$$

Eigenvalues show how well each eigenvector captures the original data in L^2 sense. Eigenvectors of matrix R can be found using Singular Value Decomposition (SVD) of matrix P :

$$P = \Phi \Sigma \Psi^T \quad (\text{S11})$$

where in general $\Phi \in \mathbb{R}^{2N_x N_y \times 2N_x N_y}$ and $\Psi \in \mathbb{R}^{N_d \times N_d}$ are orthogonal ($\Phi \Phi^T = I_{2N_x N_y \times 2N_x N_y}$ and $\Psi \Psi^T = I_{N_d \times N_d}$) and determine, through columns, the left and right singular vectors of P ; and diagonal matrix $\Sigma \in \mathbb{R}^{2N_x N_y \times N_d}$ has singular values on its diagonal (35). We can write:

$$\begin{aligned} R &= \frac{1}{(N_d - 1)} P P^T = \frac{1}{(N_d - 1)} \Phi \Sigma \Psi^T \Psi \Sigma^T \Phi^T \\ R \Phi &= \frac{1}{(N_d - 1)} \Phi \Sigma \Sigma^T \end{aligned} \quad (\text{S12})$$

because of the special form of Σ that will be discussed shortly, the columns of Φ (denoted here by ϕ_i and are plotted in Fig 2 for $i \leq 4$) are eigenvectors of matrix R that are ordered by the

variance they capture in data. Note that $\phi_i \in \mathbb{R}^{2N_x N_y}$ and we can separate it into eigenvectors of the slip rate (ϕ_i^V) and the state variable ϕ_i^θ :

$$\phi_i = \begin{bmatrix} \phi_i^V \\ \phi_i^\theta \end{bmatrix} \quad (\text{S13})$$

Assuming the number of time snapshots is much smaller than the dimension of the problem $N_d \ll 2N_x N_y$, Σ has the following form:

$$\Sigma = \begin{bmatrix} \sigma_1 & 0 & 0 & 0 \\ 0 & \sigma_2 & 0 & 0 \\ \vdots & \vdots & \ddots & \vdots \\ 0 & 0 & 0 & \sigma_{N_d} \\ 0 & 0 & 0 & 0 \\ \vdots & \vdots & \vdots & \vdots \\ 0 & 0 & 0 & 0 \end{bmatrix}_{2N_x N_y \times N_d} \quad (\text{S14})$$

Then, using Eqs (S10), (S12), and (S14), $\frac{1}{(N_d-1)}\sigma_j^2 = \lambda_j$. λ_j corresponds to the variance of the data along ϕ_j . If λ_j goes to zero very fast, it suggests that we can explain the dataset in a low-dimensional subspace consisting of a finite number of eigenfunctions. The ratio $\sum_{j=1}^r \lambda_j / \sum_{j=1}^{N_d} \lambda_j$ shows the proportion of the variance of the data that are captured in the first r eigenfunctions. Based on Fig S2, the first 13 modes of the data capture almost 85% of the data.

Using this explanation, we can approximate the interevent period ($\mathcal{A} \setminus E(V_{\text{thresh}})$) by:

$$\log_{10} (\mathcal{A} \setminus E(V_{\text{thresh}})) \approx \left\{ w = \bar{w} + \sum_{i=1}^{N_m} a_i \phi_i \left| \sum_{i=1}^{N_m} \frac{a_i^2}{\lambda_i} \leq r_0^2 \right. \right\}. \quad (\text{S15})$$

where N_m is the number of modes (eigenfunctions) that are considered in the truncation. One can play with r_0 to enlarge the set. For very large r_0 the approximation is not valid anymore. The value of r_0 determines how much we let perturbation around the average of the dataset \bar{w} . As an example, taking $N_m = 1$ and $r_0 = 1$ would let perturbation around \bar{w} along ϕ_1 with an amplitude equal to the standard deviation of the dataset along that eigenvector ($\sqrt{\lambda_1}$).

Using the orthonormality of ϕ_i 's, we can find the projection of any $w(t)$ onto ϕ_i using the following inner product:

$$a_i(t) = \langle w(t) - \bar{w}, \phi_i \rangle \quad (\text{S16})$$

where $a_i(t)$ is the projection of $w(t) - \bar{w}$ onto eigenvector ϕ_i and \langle, \rangle denotes the inner product. We can find $a_i(t_k)$ for all of the time snapshots in the dataset and plot the distribution of $a_i/\sqrt{\lambda_i}$ (Fig S3). We see that the distribution is close to the standard normal distribution. Looking at this figure gives us intuition about choosing a value for r_0 . For example, selecting r_0 to be large (> 4), would lead to exploring low-probability regions. The dashed lines in the figure, correspond to $a_i/\sqrt{\lambda_i} = 1, 2, 3$.

Using the approximation in Eq (S15), we reduce the dimensionality of the system from $\mathbb{R}^{2N_x N_z}$ to \mathbb{R}^{N_m} and approximate a complicated set ($\mathcal{A} \setminus E(V_{\text{thresh}})$) by a hyperellipse which is a straightforward constraint for our optimization problem. With the mentioned approximation, and denoting $w^* = \bar{w} + \sum_{i=1}^{N_m} a_i^* \phi_i$, we write an optimization problem in the low dimensional \mathbb{R}^{N_m} space which is an equivalent approximate of Eq (7):

$$A^* = \left\{ \mathbf{a}^* \mid \sum_{i=1}^{N_m} \frac{a_i^{*2}}{\lambda_i} \leq r_0^2, w^* \text{ is a local maximizer of } F(10^{w^*}; \Delta t, T), F(10^{w^*}; \Delta t, T) > F_e^* \right\} \quad (\text{S17})$$

where $\mathbf{a}^* \in \mathbb{R}^{N_m}$ whose i^{th} element is a_i^* . Eq (S17) ensures that the optimal solutions are not too far from the mean states (\bar{w}).

To show the applicability of the POD model reduction outside the application of this paper, we also applied the method to a dataset including all snapshots within the period of 200 years to 1200 years (without removing the event period). The result of this model reduction is available in Supplemental Video 2. This video shows that we can capture all phases of earthquake cycles using a few POD modes.

Supp C Optimization

Here we revisit optimal sampling in the framework of Bayesian optimization as discussed in (41) and is improved in (40) for finding the precursors of extreme events. The optimization algorithm works by exploring the input space ($\mathbf{a} = [a_1, \dots, a_{N_m}] \in \mathbb{R}^{N_m}$) using a Gaussian surrogate model. Suppose that we want to solve the constrained optimization problem of Eq (7) with the approximation in Eq (8). Without loss of generality, we study the minimization of the minus sign of the cost function ($G = -F$) instead of maximizing it. The cost function can be evaluated using a forward simulation of a given initial condition. Here we assume that the observation is contaminated by a small Gaussian noise with variance $\sigma_\epsilon^2 = 10^{-4}$.

$$z = G(a; T, \Delta t) + \epsilon \quad \epsilon \sim \mathcal{N}(0, \sigma_\epsilon^2) \quad (\text{S18})$$

where ϵ is the observational noise, and T and Δt are hyperparameters of the cost function G that are determined before the optimization process. The iterative approach starts from some randomly sampled N_{init} points $\{\mathbf{a}_k \in \mathbb{R}^{N_m}\}_{k=1}^{N_{init}}$ that each of them corresponds to a point in the set defined in (8). Using the forward model of Eq (S18) we find the input-output pair $\mathcal{D}_0 = \{\mathbf{a}_k, z_k\}_{k=1}^{N_{init}}$. $\mathbf{a}_k \in \mathbb{R}^{N_m}$ is the vector of POD coefficients with N_m as the number of POD modes we have decided to consider, and z_k comes from Eq (S18). Using a Gaussian surrogate model, the expected value and variance of the process, condition on the input/output at each step i (\mathcal{D}_i) is given by the following equation:

$$\begin{aligned} \mu(\mathbf{a}) &= m_0 + k(\mathbf{a}, \mathbf{A}_i) \mathbf{K}_i^{-1} (\mathbf{z}_i - m_0) \\ \sigma^2(\mathbf{a}) &= k(\mathbf{a}, \mathbf{a}) - k(\mathbf{a}, \mathbf{A}_i) \mathbf{K}_i^{-1} k(\mathbf{A}_i, \mathbf{a}) \end{aligned} \quad (\text{S19})$$

where $\mathbf{K}_i = k(\mathbf{A}_i, \mathbf{A}_i) + \sigma_\epsilon^2 \mathbf{I}$, $\mathbf{A}_i = \{\mathbf{a}_k\}_{k=1}^{N_{init}+i}$, and $\mathbf{z}_i = \{z_k\}_{k=1}^{N_{init}+i}$. We consider the Radial Basis Function (RBF) with Automatic Relevance Determination (ARD):

$$k(\mathbf{a}, \mathbf{a}') = \sigma_f^2 \exp(-(\mathbf{a} - \mathbf{a}')^T \Theta^{-1} (\mathbf{a} - \mathbf{a}') / 2) \quad (\text{S20})$$

where Θ is a diagonal matrix containing the length scale for each dimension. At each iteration, we construct a surrogate model (Eq (S19)). Then, the next point in the input space is found by minimizing an acquisition function ($g : \mathbb{R}^{N_m} \rightarrow \mathbb{R}$). We use the **Lower Confidence Bound** (LCB) acquisition function which is defined as the following:

$$g_{LCB}(\mathbf{a}) = \mu(\mathbf{a}) - \kappa\sigma(\mathbf{a}) \quad (\text{S21})$$

where κ is a positive number that balances exploration and exploitation. For small κ , we do not consider uncertainties of the surrogate model and trust the mean of the conditional Gaussian process. For large κ , minimizing Eq (S21) is equivalent to finding a point that has the largest uncertainty. We use $\kappa = 1$ in this study. The algorithm is extracted from Ref (40) and is summarized in Algorithm 1. We start the algorithm by randomly sampling 10 initial points inside the hyper-ellipse (Eq (8)) and then augmenting the input-output pairs by minimizing the acquisition function until the size of the input-output points reaches 200. To show the effectiveness of the algorithm in finding optimal solutions, we define the function c as the following:

$$c(i) = - \min_{1 \leq j \leq i} \min_{\mathbf{a}} \mu(\mathbf{a} | \mathcal{D}_j) \quad (\text{S22})$$

To find $c(i)$, we need to find the minimum of the Gaussian process in each iteration i and report the minimum over all $1 \leq j \leq i$. The algorithm does not guarantee finding all of the local maxima. As a result, the algorithm is repeated for 30 trials with different randomly chosen initial points. The behaviour of $c(i)$ for different values of r_0 is plotted in Fig S4 (a). The solid line is the median of $c(i)$ for different trials as a function of iteration and the shaded band shows half of the median absolute deviation. One of the optimal solutions is plotted in Fig S4 (b,c). During the optimization process, we augment the set W^* if the condition in Eq (9) is satisfied.

Algorithm 1 Bayesian Optimization

- 1: **Input:** Number of initial points n_{init} and number of iterations n_{iter}
- 2: **Initialize:** Surrogate model on initial dataset $\mathcal{D}_0 = \{\mathbf{a}^{(k)}, z^{(k)}\}_{k=1}^{n_{init}}$
- 3: **for** $n=0$ to n_{iter} **do**
- 4: Select best next point \mathbf{a}_{n+1} by minimizing acquisition function constrained inside the hyperellipse (Eq (8)):

$$\mathbf{a}^{(n+1)} = \arg \min_{\sum_{i=1}^{N_m} \frac{a_i^2}{\lambda_i} \leq r_0^2} g_{LCB}(\mathbf{a}; \bar{G}, \mathcal{D}_n)$$

- 5: Evaluate objective function G at $\mathbf{a}^{(n+1)}$ and record $z^{(n+1)}$
 - 6: If $z^{(n+1)} < -F_e^*$ augment the set W^* (Eq (9))
 - 7: Augment dataset $\mathcal{D}_{n+1} = \mathcal{D}_n \cup \{\mathbf{a}_{n+1}, z_{n+1}\}$
 - 8: Update surrogate model
 - 9: **end for**
-

Supp D Forecast with Partial Observation of Slip Rate

So far, we have assumed that we have full access to the slip rate on the fault. Here, we relax this assumption and use slip rate measurements only at a few points on the fault (diamonds in Fig 1 (a)). We denote $\hat{V} : \mathbb{Z}^{N_p} \times \mathbb{R}^+ \rightarrow \mathbb{R}^+$ as the time series of partial slip rate observation, where N_p is the number of points of slip rate measurements and we take it to be 16 in this case study. We assume that these points are at the center of the fault along the depth and have equal distances along the strike. We redefine the indicator $I(t)$ for this special case as follows:

$$I(t) = \max_i \frac{\langle \log \hat{V}(t) - \hat{w}^V, \log \hat{V}_i^* - \hat{w}^V \rangle_{\mathbb{R}^{N_p}}}{\| \log \hat{V}(t) - \hat{w}^V \|_2 \| \log \hat{V}_i^* - \hat{w}^V \|_2} \quad (\text{S23})$$

where \hat{V}_i^* is the slip rate at the measurement points (diamonds in Fig 1 (a)) of the i^{th} optimal solution in the set W^* . \hat{w}^V is the average slip rate at the measurement points during the interevent period. $\langle \cdot, \cdot \rangle_{\mathbb{R}^{N_p}}$ is the inner product in \mathbb{R}^{N_p} . Fig S5 shows the forecast performance in the limited slip rate measurement scenario. The general consistent increase in $I(\cdot)$ when the function $F(\cdot)$ rises is visible in Fig S5 (a). Fig S5 (b) and (c) show statistically the performance of the predictor. While most of the probability mass of $P(F|I)$ belongs to true positive and true negative we should appreciate that there is more probability mass in the false positive quadrant compared to the scenario in which we have full access to the slip rate. This can be observed better in Fig S5 (c), (d), and (e). Although as I increases, P_{ee} increases consistently, P_{ee} is almost 0.9 when I is the maximum which suggests that there is a 10% chance of a false positive signal when I takes its maximum value. This false positive can also be observed in Fig S5 (d) and (e) around the year 1610. While it is important to appreciate the limitations, the overall performance is satisfying. To reduce this limitation, one can use filtering methods to invert and approximate slip rates at a few more points on the fault to improve the performance.

Supplemental Figures

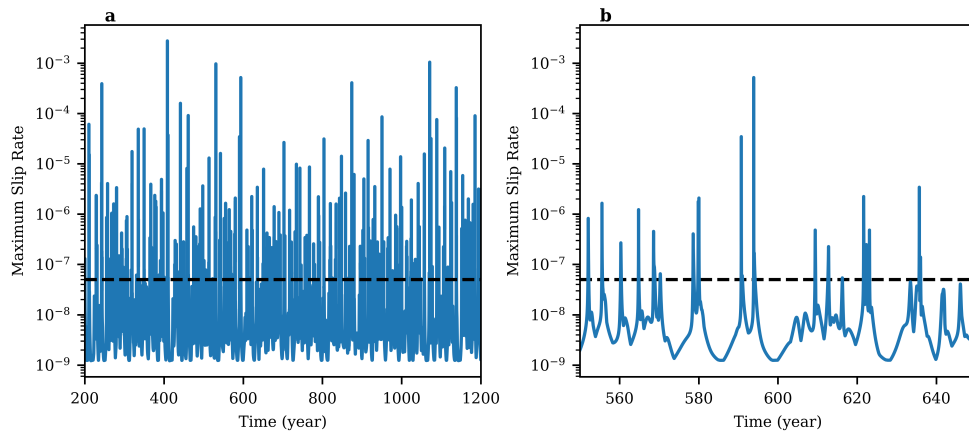


Figure S1: Time series of the maximum slip rate for a period of 1000 years (a) and 100 years (b) with threshold velocity denoted by a dashed line.

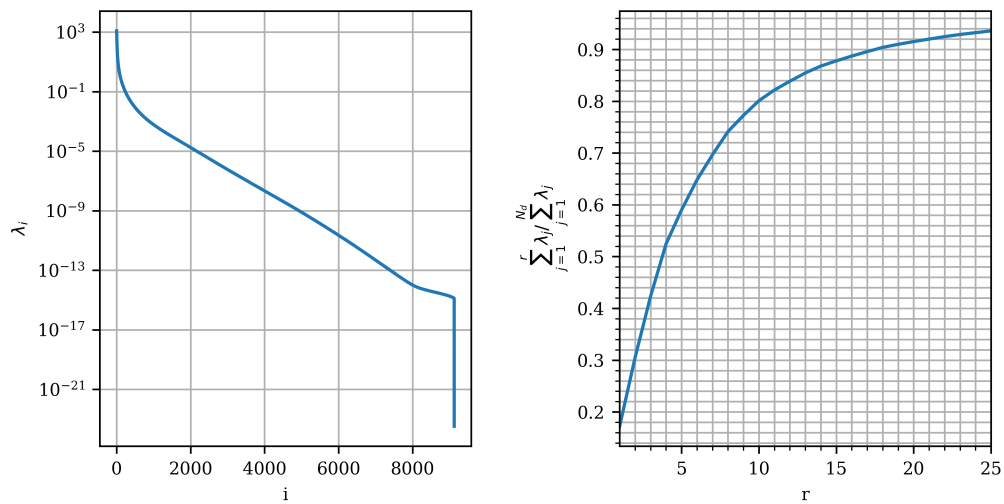


Figure S2: Convergence of the eigenvalues (left) and the ratio of a truncated sum of eigenvalues to the total sum of eigenvalues (right).

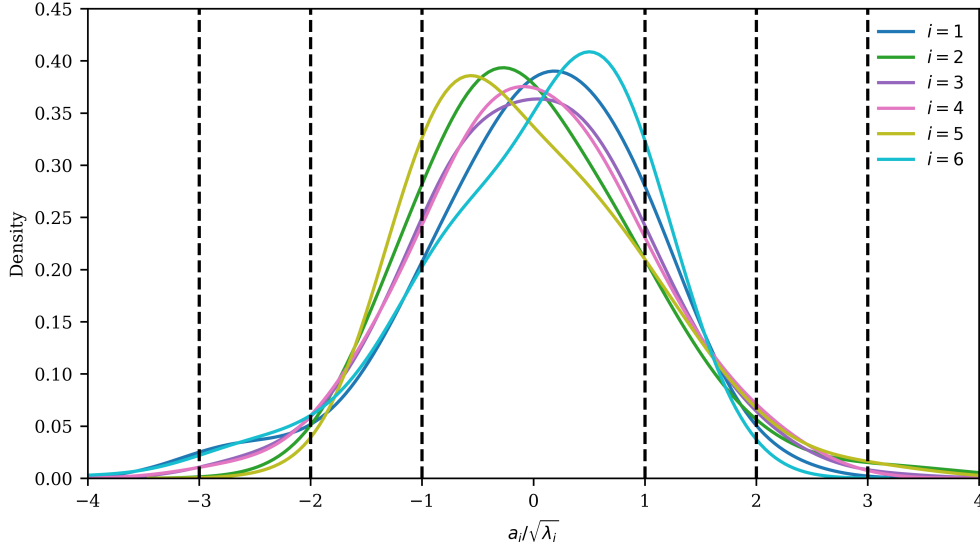


Figure S3: The distribution of $a_i(t)/\sqrt{\lambda_i}$ in the dataset of the interevent periods. The vertical lines correspond to $a_i/\sqrt{\lambda_i} = \pm 1, \pm 2, \pm 3$ and are plotted to give insight for selecting proper r_0 in Eq (8)

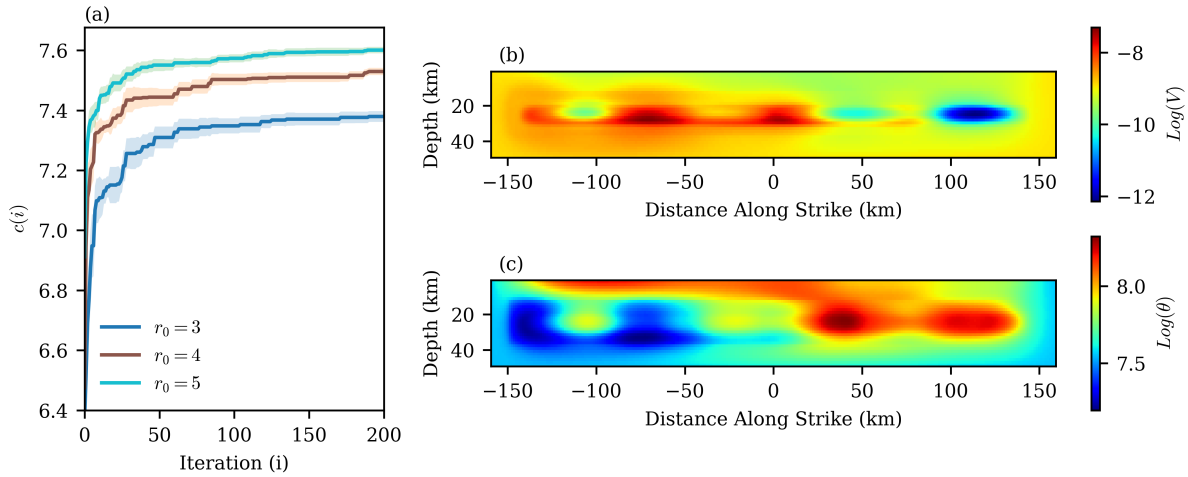


Figure S4: Convergence of the optimization for different values of r_0 (a). $\log_{10}(V)$ and $\log_{10} \theta$ of one of the optimal solutions with $r_0 = 3$ which leads to a magnitude 7.5. The optimal solution is highly heterogeneous and shows the effect of favorable stress heterogeneity in generating big events (b,c). The stress calculated from this optimal solution is plotted in 3

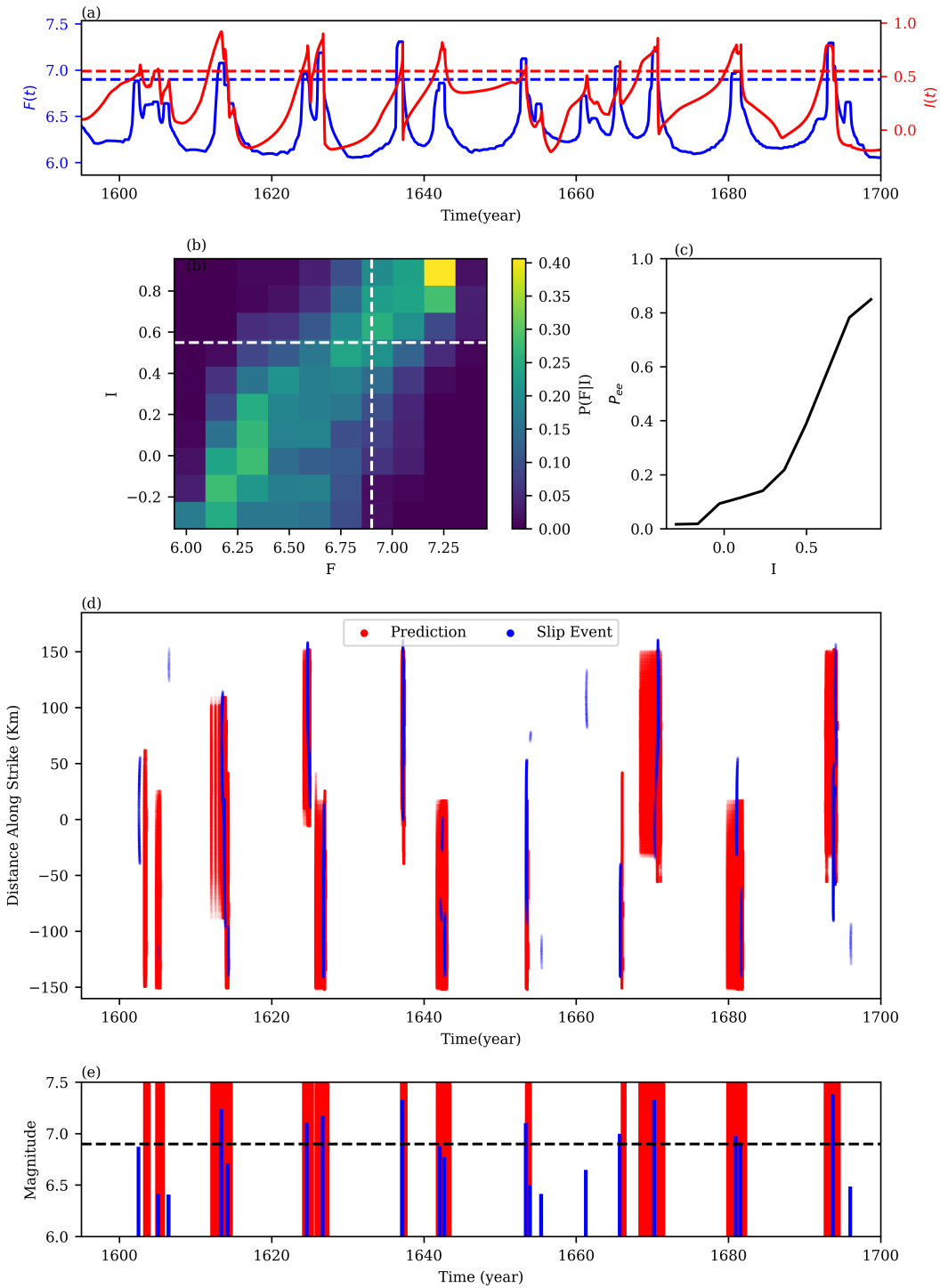


Figure S5: Spatio-temporal prediction of events same as in Fig 4 but using slip rate only at 16 points on the fault (denoted in Fig 1 (a) by diamonds)